Journal of The Electrochemical Society

The Electrochemical Society
Advancing solid state & electrochemical science & technology

OPEN ACCESS

# Simulating the Influence of Supporting Electrolyte Concentration on Copper Electrodeposition in Microvias

To cite this article: T. M. Braun *et al* 2022 *J. Electrochem. Soc.* **169** 012502

*Journal of The Electrochemical Society*, 2022 **169** 012502

# Simulating the Influence of Supporting Electrolyte Concentration on Copper Electrodeposition in Microvias

**T. M. Braun,[1,*,z] J. John,[2] N. Jayaraju,[2] D. Josell,[1] and T. P. Moffat[1,**]**

[1]*Materials Science and Engineering Division, National Institute of Standards and Technology, Gaithersburg, Maryland, United States of America*
[2]*DuPont Electronics & Imaging, Marlborough, Massachusetts, United States of America*

Robust, void-free Cu electrodeposition in high-aspect ratio features relies on careful tuning of electrolyte additives, concentrations, and electrochemical parameters for a given feature dimension or wafer pattern. Typically, Cu electrodeposition in electronics manufacturing of microscale or larger features (i.e., microvias, through-holes, and high-density interconnects) employs a $CuSO_4$–$H_2SO_4$ electrolyte containing millimolar levels of chloride and, at a minimum, micromolar levels of a polyether suppressor. Research and optimization efforts have largely focused on the relationship between electrolyte additives and growth morphology, with less attention given to the impact of supporting electrolyte. Accordingly, a computational study exploring the influence of supporting electrolyte on Cu electrodeposition in microvias is presented herein. The model builds upon prior experimental and computational research on localized Cu deposition by incorporating the full charge conservation equation with electroneutrality to describe potential variation in the presence of ionic gradients. In accord with experimental observations, simulations predict enhanced current localization to the microvia bottom as $H_2SO_4$ concentration is decreased. This phenomenon derives from enhanced electromigration within recessed features that accompanies the decrease of conductivity with local metal ion depletion. This beneficial aspect of low acid electrolytes is also impacted by feature density, $CuSO_4$ concentration, and the extent of convective transport.

 [DOI: 10.1149/1945-7111/ac4845]

Manuscript submitted November 13, 2021; revised manuscript received December 19, 2021. Published January 18, 2022.

Electrodeposition is widely used for filling high-aspect ratio recessed features to fabricate Cu interconnects that range in scale from nanometer-scale wiring in integrated circuits to micrometer-scale through-silicon vias for chip stacking and millimeter-scale features in high density printed circuit boards. Typically, multi-component additive packages (i.e., suppressor, accelerator, and leveler) are used to achieve robust filling of recessed features, ranging from trenches and vias to through-holes.[1–12] Feature filling in the presence of such additive packages derives from competitive adsorption of species that accelerate or inhibit metal deposition kinetics coupled with variation in surface coverages that accompany changes in surface area.[1–3] When the feature dimensions approach or exceed the thickness of the hydrodynamic boundary layer, the effect of metal ion and additive depletion gradients become important factors in the filling behavior. For deposition under such conditions, electrolytes employing a single suppressing additive are able to yield robust, bottom-up electrodeposition in through-silicon via (TSV) and through-hole (TH) features.[13–20] Here, preferential bottom-up filling follows from selective breakdown of the inhibition adlayer at the most recessed region of the feature. In the case of Ni,[21,22] Co,[23] and Au[24,25] only a single additive is necessary to generate this form of highly localized deposition. In contrast, suppression of Cu deposition requires co-adsorption of the suppressor molecule, typically a polyether, with halide.[20,26–43] Polarization to sufficiently negative potentials disrupts the chloride-polyether adlayer, permitting $Cu^{2+}$ access to the electrode for active electrodeposition.[14–16,42–47]

In addition to applied potential, adlayer formation and breakdown depends on additive transport in the cell (i.e., diffusion, electromigration, and convection) and thus is directly correlated to system parameters such as additive concentrations,[16] supporting electrolyte content,[11] and agitation.[48] Adlayer breakdown involves a combination of desorption, deactivation, and/or incorporation of additive components into the metal deposit. It is also possible, although not yet fully explored, that metal deposition supports suppressor deactivation by preventing additive adsorption on the comparatively rapidly advancing active interface.[15] In cyclic voltammetry measurements, potential-driven breakdown results in a sharp increase in deposition current that is sustained through the return sweep, producing significant hysteresis in the i-V response. Correcting for the ohmic losses in the electrochemical cell gives a voltammogram with an S-shaped negative differential resistance (S-NDR), where a decrease in driving force (overpotential) is associated with an increase in reaction rate (current). Operating at applied potentials within the hysteretic region leads to bifurcation of the electrode surface into active and passive reaction zones. On macroscale electrodes this leads to the development of Turing patterns[15,49–54] whereas on topographically varied electrodes active deposition can be localized within features.[13–20,47,48,55] For high-aspect ratio TSVs and THs in particular the bifurcation is such that the planar field is passive due to a higher inhibitor flux while active deposition occurs in the more remote regions of recessed features. Nonetheless, the growth dynamics on both planar and patterned surfaces are related, deriving from the differing time-scale between the rapid electrical response and more sluggish evolution of chemical gradients.

Significantly, the electrical response couples through electromigration to chemical gradients that also drive diffusion and, sometimes, forced convection. This relationship leads to dependence of morphological evolution and electrode bifurcation on the control mode and uncompensated cell resistance.[56,57] For galvanostatic (or galvanodynamic) control the filling profile is often independent of the magnitude of global cell resistance.[57] In contrast, in the absence of significant ohmic losses, potential control within the hysteretic region is unstable as the entire electrode tends to jump to either the active or passive deposition branch. For potentiostatic control the addition of uncompensated resistance to the electrochemical cell can result in significant perturbation of the growth modalities during feature filling, including robust, void-free filling profiles that are impossible to obtain with lower levels of uncompensated resistance.[57] The presence of such resistance provides a stable, single valued control point at which the electrode can bifurcate into passive and active regions. In-situ optical microscopy during cyclic voltammetry and linear galvanodynamic sweeps on microelectrodes with well-defined electrical and chemical transport fields enable this behavior to be captured visually.[56] During voltammetry, the microelectrode rapidly shifts from the passive to the active state when the

*Electrochemical Society Member.
**Electrochemical Society Fellow.
[z]E-mail: trevor.braun@nist.gov

potential is swept to sufficiently negative values to disrupt the polyether-halide adlayer. In contrast, galvanodynamic measurements demonstrate more control over electrode bifurcation into active and passive zones until eventually the applied current is high enough to activate the entire electrode interface.

A recent computational study exploring the influence of uncompensated resistance on feature filling demonstrates[57] how the global cell resistance can affect growth morphology during deposition under potentiostatic control. However, several studies have also noted a change in filling behavior as the supporting electrolyte concentration, a parameter that impacts both the global cell resistance and the local electrical and chemical gradients, is varied.[11,58,59] Previous computational modeling of Cu electrodeposition for feature filling applications typically assumes a constant electrolyte conductivity and employs Laplace's equation to describe potential gradients in solution. While this approach is an effective approximation for systems with a high supporting electrolyte concentration and/or low reactant depletion, the need for speed in industrial applications motivates the exploration of electrodeposition near the transport limit of the metal ion reactant. Accordingly, the present study explores the influence of supporting electrolyte concentration in the $CuSO_4$–$H_2SO_4$ system on the evolution of the local electrical and chemical gradients and their impact on transport of $Cu^{2+}$ and other charge bearing species, including additives, on deposition in microvias. These calculations employ the full charge conservation equation, with electroneutrality and potential variation in the presence of significant ionic gradients naturally giving rise to local variations in the solution conductivity. The computations are built upon a suppressor co-adsorption S-NDR model that has previously been shown to capture electroanalytical measurements and feature filing dynamics across a range of electrolytes and electrode geometries.[16,48,56,57,60] This study explores galvanostatic control because feature filling dynamics within the suppressor-based S-NDR construct in this case were previously shown to be independent of the *global* cell resistance, permitting a more direct correlation between changes to the *local* microenvironment and the fill profile. Importantly, the simulations demonstrate enhanced current localization to the bottom of the microvia (or TSV) as sulfuric acid concentration is decreased, a result that is in accord with experimental observation. This phenomenon is directly related to enhanced transport by electromigration within the via relative to the field that occurs when metal ion is significantly depleted. The disparity in *local* electromigration between the field and within the via is doubly beneficial for bottom-up filling; the negatively charged chloride (adlayer component) experiences increased transport *away from* the electrode while the positively charged cupric ion (adlayer disruptor) is subject to enhanced chemical transport *towards* the electrode. The filling advantage observed with decreasing $H_2SO_4$ concentration is shown to depend on the feature array density as well as the extent of diffusive/convective transport. Furthermore, in electrolytes with low concentrations of $H_2SO_4$, significant cupric ion depletion is necessarily accompanied by a parallel decrease in the sulfate anion concentration due to electroneutrality, which further shifts the pH and bisulfate concentration through the homogeneous reaction to maintain their local equilibrium. Although not the focus of the present work, it is also possible that significant chemical interactions occur between the supporting electrolyte (i.e., non-reacting species) and the solvation/desolvation of $Cu^{2+}$, $Cu^{+}$, and/or adsorbed additives at the interface; however, probing such questions will require further analytical measurements of the relevant chemical relationships.

## Computational Methods

Finite element method (FEM) computations are used to simulate copper electrodeposition in microscale vias (i.e., blind vias, TSV, etc). The dimensions of the microvia and the cylindrically symmetric cell centered around it in the present model are: radius $R_{via} = 25\ \mu m$, height $H_{via} = 60\ \mu m$, and cell radius $R_c = 75\ \mu m$ or $750\ \mu m$. A reference electrode and counter electrode are combined in a common plane at a distance $L_{RE}$ above the microvia surface (i.e., field). A boundary layer thickness $\delta$ is used to approximate the diffusion field in the axisymmetric cell that would be associated with convective flow; a 10 $\mu$m boundary layer thickness corresponds to approximately a 1600 rpm (3200 $\pi$ rad·min$^{-1}$) rotation rate of a rotating disk electrode for typical electrolyte viscosity in the Levich theory.[61] Electrolyte occupies the internal volume of the cell with the concentration $C_i$ and flux $N_i$ of each species ($Cu^{2+}$, $SO_4^{2-}$, $H^+$, $HSO_4^-$, $Na^+$, $Cl^-$, and $TET^{2+}$) solved within the electrolyte domain in accord with the Nernst-Planck equation, excluding convection,

$$\frac{dC_i}{dt} = -\nabla \vec{N}_i = -\nabla(-z_i u_{m,i} F C_i \nabla\phi - D_i \nabla C_i) \quad [1]$$

given Faraday's constant $F$ and the species' charges $z_i$, diffusion coefficients $D_i$, and mobilities $u_{m,i}$ calculated by the Einstein relationship

$$u_{m,i} = \frac{D_i}{RT} \quad [2]$$

The simulated electrolyte assumes full dissociation of $CuSO_4$ into $Cu^{2+}$ and $SO_4^{2-}$ and NaCl into $Na^+$ and $Cl^-$. Speciation of the supporting electrolyte, $H_2SO_4$, is calculated accounting for bisulfate dissociation

$$H^+ + SO_4^{2-} \leftrightarrow HSO_4^- \quad [3]$$

using the equilibrium constant ($K_3$) and adjusting for the ionic strength, $I_s$, of the electrolyte[62,63]

$$K_3 = \frac{C_{HSO4}}{C_H C_{SO4}} = log(K_3^o) - \frac{2.036 I_s^{0.5}}{(1 + 0.52 I_s^{0.5})} \quad [4]$$

where $K_3^o$ is the equilibrium constant in the dilute limit and the ionic strength is defined by

$$I_s = 0.5 \sum z_i^2 C_i \quad [5]$$

The Tetronic 701[a] suppressor is assumed to be doubly protonated (2+) in the low pH solutions.[64] Diffusion coefficients listed in Table I for each species are estimated from literature sources.[16,65–69]

Current density $\vec{j}$ is associated with the ionic flux $\vec{N}_i$ through the electrolyte

$$\vec{j} = F \sum z_i \vec{N}_i \quad [6]$$

Using the expressions for $\vec{N}_i$ from Eq. 1 allows Eq. 6 to be rewritten in the form

$$\vec{j} = -\kappa \nabla\phi - F \sum z_i D_i \nabla C_i \quad [7]$$

with the electrical conductivity, $\kappa$, thus related to the ionic charges, mobilities and concentrations according to

$$\kappa = F^2 \sum z_i^2 u_{m,i} C_i \quad [8]$$

With the assumption of electroneutrality throughout the solution volume,

$$\sum z_i C_i = 0 \quad [9]$$

the potential is solved throughout the volume of the electrolyte subject to conservation of charge

[a]Identification of commercial products in this paper is done to specify the experimental procedure. In no case does this imply endorsement or recommendation by the National Institute of Standards and Technology (NIST).

**Table I. Parameters for microvia simulations.**

| Parameter | Name | Units | Value | References |
|---|---|---|---|---|
| | | *Electrochemical Cell Geometry* | | |
| Microvia radius | $R_{via}$ | $\mu$m | 25 | — |
| Microvia height | $H$ | $\mu$m | 60 | — |
| Cell radius | $R_c$ | $\mu$m | 75–750 | — |
| Boundary layer thickness | $\delta$ | $\mu$m | 10 | — |
| Reference/counter electrode distance | $L$ | cm | 0.25 | — |
| | | *Electrolyte Parameters* | | |
| Bulk concentration $CuSO_4$ | $C^o_{Salt}$ | $mol \cdot l^{-1}$ | 0.44–1 | — |
| Bulk concentration of $H_2SO_4$ | $C^o_{Acid}$ | $mol \cdot l^{-1}$ | 0.01–0.8 | — |
| Bulk concentration $Cl^-$ | $C^o_{Cl}$ | $mmol \cdot l^{-1}$ | 1 | — |
| Bulk concentration polyether (Poloxamine Tetronic 701) | $C^o_P$ | $\mu mol \cdot l^{-1}$ | 25 | — |
| Diffusion coefficient of $Cu^{2+}$ | $D_{Cu}$ | $cm^2 \cdot s^{-1}$ | $5 \times 10^{-6}$ | Ref. 65 |
| Diffusion coefficient of $SO_4^{2-}$ | $D_{SO4}$ | $cm^2 \cdot s^{-1}$ | $6.9 \times 10^{-6}$ | |
| Diffusion coefficient of $H^+$ | $D_H$ | $cm^2 \cdot s^{-1}$ | $6 \times 10^{-5}$ | |
| Diffusion coefficient of $HSO_4^-$ | $D_{HSO4}$ | $cm^2 \cdot s^{-1}$ | $8.6 \times 10^{-6}$ | |
| Diffusion coefficient $Cl^-$ | $D_{Cl}$ | $cm^2 \cdot s^{-1}$ | $9 \times 10^{-6}$ | Ref. 16 |
| Diffusion coefficient $Na^+$ | $D_{Na}$ | $cm^2 \cdot s^{-1}$ | $8.6 \times 10^{-6}$ | |
| Diffusion coefficient polyether (Poloxamine Tetronic 701) | $D_P$ | $cm^2 \cdot s^{-1}$ | $1 \times 10^{-6}$ | Refs. 67–69 |
| Ionic charge of polyether | $z_{TET}$ | — | 2 | |
| Reversible Potential | $E_{rev}$ | V | -0.38 | *Measured* |
| | | *Adsorbate Parameters* | | |
| Saturation chloride coverage | $\Gamma_{Cl}$ | $mol \cdot m^{-2}$ | $1.62 \times 10^{-5}$ | Ref. 16 |
| Saturation suppressor coverage | $\Gamma_P$ | $mol \cdot m^{-2}$ | $9.8 \times 10^{-8}$ | Ref. 64 |
| Chloride adsorption kinetics | $k^+_{Cl}$ | $m^3 \cdot (mol \cdot s)^{-1}$ | 20 | Ref. 16 |
| Chloride deactivation kinetics | $k^-_{Cl}$ | $m^{-1}$ | $1.5 \times 10^7$ | Ref. 16 |
| Suppressor adsorption kinetics | $k^+_P$ | $m^3 \cdot (mol \cdot s)^{-1}$ | 50 | Ref. 16 |
| Suppressor deactivation kinetics | $k^-_P$ | $m^{-1}$ | $5 \times 10^4$ | Ref. 16 |
| Initial chloride & polymer coverages | $\theta_{i,o}$ | | 1 | |
| | | *Electrochemical Kinetics* | | |
| Unsuppressed Cu exchange current density | $j^o_0$ | $A \cdot m^{-2}$ | 24 | *Measured* |
| Suppressed Cu exchange current density | $j^o_1$ | $A \cdot m^{-2}$ | 0.014 | *Measured* |
| Unsuppressed charge transfer coefficient | $\alpha_0$ | – | 0.7 | *Measured* |
| Suppressed charge transfer coefficient | $\alpha_1$ | – | 0.7 | *Measured* |
| Cu ionic charge | $n$ | – | 2 | — |
| Cu molar volume | $\Omega$ | $m^3 \cdot mol^{-1}$ | $7.1 \times 10^{-6}$ | — |
| Temperature | $T$ | K | 298 | — |
| | | *Homogeneous Reactions* | | |
| Sulfate—bisulfate equilibrium constant | $K^o_3$ | $l \cdot mol^{-1}$ | 96.15 | |

$$\nabla \vec{j} = 0 \quad [10]$$

such that $\vec{j}$ defined by Eq. 7 results in

$$\nabla(\kappa \nabla) + F \sum z_i \nabla(D_i \nabla C_i) = 0 \quad [11]$$

***Boundary conditions.***—Accumulation of adsorbates on the electrode follows Langmuir adsorption kinetics with deactivation of suppression related to metal deposition through some combination of adsorbate desorption and/or incorporation in the deposit; the present study assumes adsorbates are only removed via incorporation. Evolution of the fractional chloride coverage $\theta_{Cl}$, defined as the local areal density of adsorbates on the surface divided by the saturation coverage, arising from the additive flux onto the surface minus the adsorbate removed from the surface is described by

$$\frac{d\theta_{Cl}}{dt} = k^+_{Cl} C_{Cl}(1 - \theta_{Cl}) - k^-_{Cl} \theta_{Cl} v \quad [12]$$

where $k^+_{Cl}$ is the adsorption rate constant, $C_{Cl}$ is the chloride concentration at the evolving metal/electrolyte interface, $k^-_{Cl}$ is the deactivation rate constant, and $v$ is the metal deposition rate. Evolution of the fractional poloxamine coverage $\theta_P$ is described analogously by

$$\frac{d\theta_P}{dt} = k^+_P C_P(\theta_{Cl} - \theta_P) - k^-_P \theta_P v \quad [13]$$

where the poloxamine is thus additionally restricted to adsorption on top of halide covered sites and thereby implicitly subject to the requirement that $\theta_P$ cannot exceed $\theta_{Cl}$ through adsorption. The fractional chloride and poloxamine coverages are further limited to values between 0 and 1. Values for $k_i^+$ and $k_i^-$ listed in Table I are estimated from model fits to the S-NDR voltammetry in additive-containing 1 $mol \cdot l^{-1}$ $CuSO_4$ + 0.5 $mol \cdot l^{-1}$ $H_2SO_4$ with the fitting procedure focused on capturing the potential dependence of suppression breakdown on the suppressor and halide concentrations.[16,45]

The metal deposition rate is a linear combination of growth on adsorbate-free (unsuppressed) and adsorbate saturated (suppressed)

areas the latter being captured by the suppressor coverage $\theta_P$ (equivalently the coverage of the polyether-chloride bi-layer) and proportional to the metal ion concentration $C_{Cu}$ adjacent to the interface

$$v(\theta_P, C_{Cu}, \eta) = \frac{\Omega}{nF}\frac{C_{Cu}}{C^o_{Cu}}[j_{\theta=0}(\eta)(1-\theta_P) + j_{\theta=1}(\eta)\theta_P] \quad [14]$$

The current densities on the unsuppressed ($j_{\theta=0}$) and suppressed ($j_{\theta=1}$) surfaces for the two electron reduction of $Cu^{2+}$ to its metallic form are translated to growth velocity, $v$, using Faraday's constant ($F = 96{,}485\ \mathrm{C\cdot mol^{-1}}$), the ionic charge $n$, and the molar volume $\Omega$ of solid copper. The current densities ($j_{\theta\ =\ 0,1}$) are assumed to exhibit the conventional Butler-Volmer exponential dependence on overpotential $\eta$ expressed as

$$j_{\theta=0,1}(\eta) = j^o_{\theta=0,1}\left(e^{\frac{(1-\alpha_{\theta=0,1})F}{RT}\eta} - e^{-\frac{\alpha_{\theta=0,1}F}{RT}\eta}\right) \quad [15]$$

The applied potential $V_{app}$ is related to the overpotential, $\eta$, at the working electrode through

$$V_{app} = \eta + \phi + E_{rev} \quad [16]$$

where the potential within the electrolyte evaluated at the electrolyte/deposit interface captures the dissipative losses due to current flow through the electrolyte between the workpiece and the reference electrode. For comparison to experimental results, the overpotential driving electrodeposition is referenced to the reversible Nernst potential for the $Cu^{2+}/Cu_{(s)}$ reaction ($E_{rev} = -0.38$ V vs saturated sulfate reference electrode). The values of $j^o_{\theta=1}$ and $\alpha_{\theta=1}$ for the fully suppressed surface are obtained by fitting the negative-going voltammetric scans up to the onset of suppression breakdown. For simplicity, the present work uses a single set of $j^o_{\theta=0}$ and $\alpha_{\theta=0}$ values for deposition on both Cl-free and Cl-covered, polymer-free unpassivated surfaces although the kinetics of metal deposition on polymer-free surfaces are known to be impacted by halide coverage.

Local charge balance requires that the current density at the electrode, extremely well approximated by that associated with the metal deposition reaction alone, be proportional to the $Cu^{2+}$ flux from the electrolyte onto the interface (outward surface normal $\hat{n}$) according to

$$\frac{1}{nF}\vec{j}\cdot\hat{n} = -(z_{Cu}u_{m,Cu}FC_{Cu}\nabla\phi + D_{Cu}\nabla C_{Cu})\cdot\hat{n} \quad [17]$$

Although the current density associated with their gradual submonolayer adsorption is negligible, local mass balance requires the normal fluxes of chloride and suppressor from the electrolyte to the interface equal the respective rates of their adsorption yielding

$$-(z_{Cl}u_{m,Cl}FC_{Cl}\nabla\phi + D_{Cl}\nabla C_{Cl})\hat{n} = \Gamma_{Cl}k^+_{Cl}C_{Cl}(1-\theta_{Cl}) \quad [18]$$

and

$$-(z_P u_{m,P}FC_P\nabla\phi + D_P\nabla C_P)\hat{n} = \Gamma_P k^+_P C_P(\theta_{Cl} - \theta_P) \quad [19]$$

with saturation coverage values $\Gamma_i$ estimated from the literature.[16,64,70,71] As stated previously, the ($\theta_{Cl}$—$\theta_P$) term captures the requirement that suppressor adsorption only occurs at chloride covered surface sites.

At the boundary layer $z = \delta$ the concentration of each species is set equal to that of the bulk solution ($C^o_i$) while the electric potential $\phi$ is set equal to $E_{rev}$ at the reference/counter electrode position 0.25 cm away from the field over the microvia. A zero-flux symmetry condition is imposed at the axisymmetric midline and at the cell edge for gradients of solution potential and concentration.

$$\left.\frac{\partial\phi}{\partial r}\right|_{r=0,R_c} = 0 \quad [20]$$

$$\left.\frac{\partial C_i}{\partial r}\right|_{r=0,R_c} = 0 \quad [21]$$

The full system of equations is solved numerically in the 2D-axisymmetric configuration using a finite element method employed in the COMSOL Multiphysics version 5.6 software package and the default solver, implementing the following modules: tertiary current distribution, separate coefficient form boundary partial differential equations for both chloride and suppressor, and deformed geometry. 2D triangular mesh elements are more highly refined along the electrode interface, initially 1.25 $\mu$m on a side. Triangular mesh elements within the boundary layer are initially no larger than 2.5 $\mu$m on each side while mesh elements outside of the boundary layer are scaled between 2.5 $\mu$m and 75 $\mu$m moving from the workpiece surface toward the reference electrode plane. Automatic remeshing is enabled, prompting re-mesh when the maximum mesh distortion parameter exceeds 4. A moving boundary smoothing parameter of 1, geometry shape order of 1, and Laplace mesh smoothing type are used in the deformed geometry module (see COMSOL documentation for detailed explanation on how these parameters impact moving boundary convergence). The system of equations is solved so that the overall charge imbalance (the fractional difference between the total integrated currents at the counter and working electrode) is less than 0.1%. The numerical evaluation error, thus, is acceptably small for the present work. To give a sense of the computational expense, typical simulations with 2300 domain and 260 boundary mesh elements take on the order of tens of minutes to compute on a Dell Precision 3630 desktop computer with an Intel Xeon E-2186G CPU @ 3.80 GHz and 64 GB RAM using Windows 10 Enterprise 64-bit operating system. More powerful computing and/or running in parallel on clusters can improve the computation time.

## Results and Discussion

This computational study is motivated by recent experimental observations of enhanced feature filling and localization of Cu deposition in solutions having lower concentrations of sulfuric acid. Figure 1a shows a series of galvanostatic through-hole (diameter = 100 $\mu$m, height = 100 $\mu$m, and pitch = 1000 $\mu$m) filling experiments at $-161\ \mathrm{A\cdot m^{-2}}$ for $\approx$ 75 min in 0.88 mol·l$^{-1}$ $CuSO_4$, 1.4 mmol·l$^{-1}$ $Cl^-$, and the indicated concentrations of $H_2SO_4$. This electrolyte also contains micromolar concentrations of a polyether suppressor, sulfur containing accelerator, and nitrogen containing leveler. Reduction of the sulfuric acid concentration from 0.6 mol·l$^{-1}$ to 0.4 mol·l$^{-1}$ causes the growth profile to transition from conformal deposition along the entire electrode to localized deposition at the TH center and filling by the "butterfly" mechanism.[17,60] Similarly, Fig. 1b shows optical micrographs of a 0.5 cm diameter rotating disk electrode after galvanostatic deposition at the indicated currents and $H_2SO_4$ concentrations while rotating at 1600 rpm in an electrolyte that further contains 0.24 mol·l$^{-1}$ $CuSO_4$, 25 $\mu$mol·l$^{-1}$ $Cl^-$, and 80 $\mu$mol·l$^{-1}$ of a polyethylene glycol (MW = 3600 g·mol$^{-1}$) suppressor. The spiral patterns develop as a result of convective flow heterogeneities that initiate on roughness and/or asperities in the mechanically polished rotating disk electrode surface.[42,50] A decrease in the $H_2SO_4$ concentration leads to spiral patterns at finer length scales indicative of enhanced localization of Cu deposition. Despite using different additive packages, both experiments presented in Fig. 1 show a clear relationship between supporting electrolyte concentration and current localization, suggesting that this trend occurs with the presence of at least a suppressing additive in solution. Because changing the sulfuric acid concentration affects

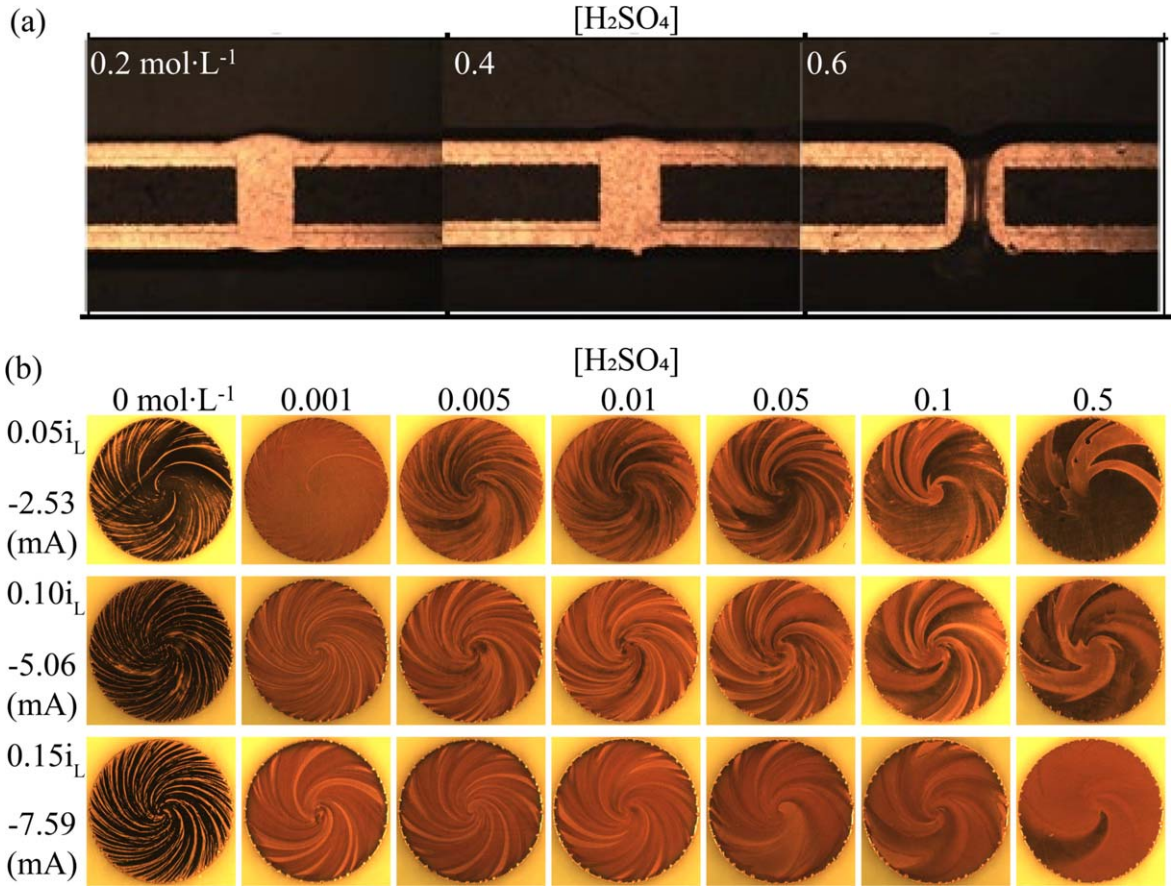


**Figure 1.** (a) Optical micrographs of galvanostatic copper electrodeposition in through-hole features (diameter = 100 $\mu$m, height = 100 $\mu$m, and pitch = 1000 $\mu$m) at $-161$ A·m$^{-2}$ for $\approx$ 75 min in 0.88 mol·l$^{-1}$ $CuSO_4$, 1.4 mmol·l$^{-1}$ $Cl^-$, and the indicated concentrations of sulfuric acid. The electrolyte also contains micromolar concentrations of polyether suppressor, sulfur containing accelerator, and nitrogen containing leveler. (b) Optical micrographs of a 0.25 cm radius rotating disk electrode (rotating at 1600 rpm) after galvanostatic deposition for 40 s at the indicated current densities and sulfuric acid concentrations in an electrolyte also containing 0.24 mol·l$^{-1}$ $CuSO_4$, 25 $\mu$mol·l$^{-1}$ $Cl^-$, and 80 $\mu$mol·l$^{-1}$ of a polyethylene glycol (MW = 3600 g·mol$^{-1}$) suppressor.

both the conductivity and the pH the experimental observations in Fig. 1 may be related to changes in the local electrical and/or chemical microenvironment. For the former case, this manifests as larger potential gradients and increased transport of ionic species by electromigration. For the latter, changes in pH and associated speciation of the sulfate/bisulfate chemistry might influence the adsorption and/or desorption of the organic additives at the electrode interface. Further still, changes in the solution pH and ionic strength may also influence the dissociation of aqueous cupric sulfate and solvation of cupric ions in solution. More extensive electroanalytical, spectroscopic studies,[72] and surface characterization measurements will be required to fully evaluate the effects of pH, sulfate, and bisulfate concentration on complexation of $Cu^{2+}$ and adsorption/desorption kinetics of the organic additives. Even absent such results, however, the prospect of enhanced electromigration at lower supporting electrolyte concentrations can be explored through computational methods and is the focus of the present study.

***Equilibrium conditions in $CuSO_4$–$H_2SO_4$ electrolytes.***—The equilibrium concentrations of $H^+$, $HSO_4^-$, $SO_4^{2-}$, $Cu^{2+}$, and $CuSO_4$(aq) can be solved using the equilibrium condition[62,63] in Eq. 4 and the equations for mass balance of the H, Cu, and S species in their various forms

$$[Cu] = [CuSO_4] = [Cu^{2+}] + [CuSO_4(aq)] \quad [22]$$

$$[H] = 2 * [H_2SO_4] = [H^+] + [HSO_4^-] \quad [23]$$

$$[S] = [H_2SO_4] + [CuSO_4] = [SO_4^{2-}] + [HSO_4^-] + [CuSO_4(aq)] \quad [24]$$

The dissociation of $CuSO_4$ versus the prospect of ion pairing has received some attention in the past.[2,66,72,73] However, in the present work $CuSO_4$ is assumed to fully dissociate into $Cu^{2+}$ and $SO_4^{2-}$, i.e., $[CuSO_4(aq)] = 0$ corresponding to an upper bound on the free cupric and sulfate ions in solution. Because the relationship in Eq. 4 is adjusted for ionic strength, solving the series of algebraic equations requires prior knowledge of the equilibrium species concentrations. Newman[66] approximates the ionic strength by assuming full dissociation of $CuSO_4$ and $H_2SO_4$ such that $I_s = 3[H_2SO_4] + 4[CuSO_4]$ given the charges of the disassociated metal, hydrogen, and sulfate ions and the definition in Eq. 5. Here, ten iterations with Newman's relationship as an initial guess of ionic strength and with the calculated concentrations as inputs for subsequent iterations were used to solve for the equilibrium species concentrations over the range of $CuSO_4$ and $H_2SO_4$ concentrations.

Figure 2a shows a color map of the electrolyte conductivity for the calculated species concentrations and diffusivities listed in Table I. Isoconductivity contour lines are included at the indicated values. As expected, solutions with a high concentration of sulfuric acid exhibit high electrical conductivity with minimal conductivity variation as copper sulfate concentration is adjusted. For example, a solution of 1 mol·l$^{-1}$ $H_2SO_4$ and 0.88 mol·l$^{-1}$ $CuSO_4$ has a conductivity of 47.9 S·m$^{-1}$ while a solution of the same acidity but

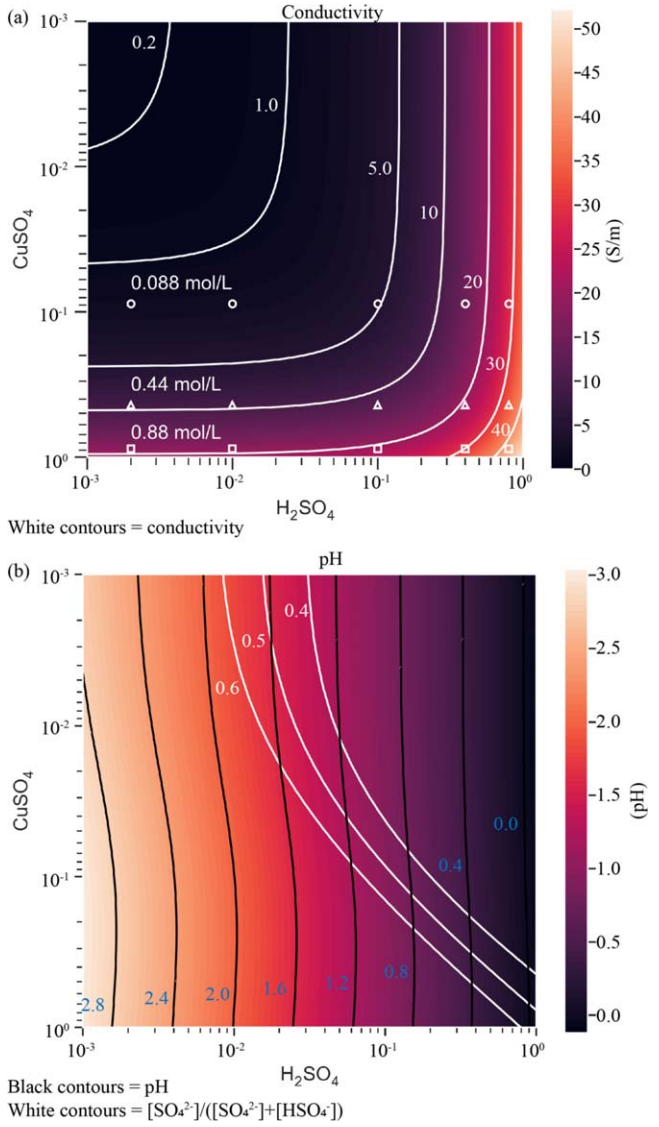


**Figure 2.** (a) Color map of calculated electrolyte conductivity for combinations of $H_2SO_4$ and $CuSO_4$ concentrations between 0.001 mol·l$^{-1}$ and 1 mol·l$^{-1}$. Isoconductivity contour lines are included at the indicated values. White squares mark solutions containing 0.88 mol·l$^{-1}$ $CuSO_4$ and 0.002, 0.01, 0.1, 0.4, or 0.8 mol·l$^{-1}$ $H_2SO_4$. White circles represent the same solutions at 90% cupric ion depletion (i.e., 0.088 mol·l$^{-1}$ $Cu^{2+}$). White triangles mark solutions containing 0.44 mol·l$^{-1}$ $CuSO_4$ for the same $H_2SO_4$ concentrations. (b) Color map of calculated pH for the same range of $H_2SO_4$ and $CuSO_4$ concentrations. Black contour lines represent constant pH at the indicated values and white contour lines show the sulfate ($SO_4^{2-}$) concentration as a fraction of the sulfate plus bisulfate ($HSO_4^-$) concentrations (i.e., the $pK_a$).

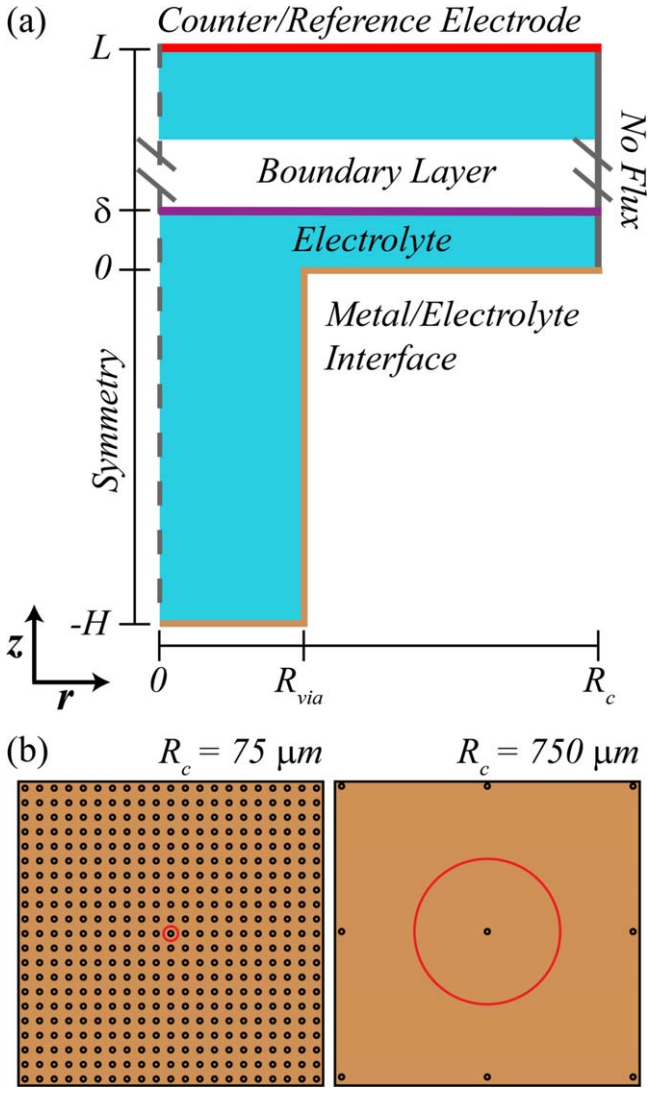


**Figure 3.** (a) Schematic of 2D-axisymmetric geometry used in the S-NDR model to simulate filling in microvias. Relevant boundaries and dimensions are indicated. Via diameter and height are 50 $\mu$m and 60 $\mu$m, respectively. The boundary layer, $\delta$, and counter/reference electrode planes are 10 $\mu$m and 0.25 cm from the microvia field, respectively. (b) Top-down schematic illustrating the corresponding high-density ($R_c$ = 75 $\mu$m) and low-density ($R_c$ = 750 $\mu$m) 2-D configurations. The red circles indicate the boundary of the computational cell in the axisymmetric simulation for each configuration. Reported workpiece current density values are determined from the applied current scaled by the projected area of the computational cell ($A_{proj} = \pi R_c^2$).

0.01 mol·l$^{-1}$ $CuSO_4$ has a conductivity of 32.8 S·m$^{-1}$ (the latter only 32% lower, or, equivalently, 0.68 as high). Solutions with low concentration of the supporting electrolyte, however, are primarily supported by the ionic content of copper sulfate. Solutions containing 0.88 mol·l$^{-1}$ and 0.01 mol·l$^{-1}$ $CuSO_4$ with 0.01 mol·l$^{-1}$ $H_2SO_4$ have solution conductivities of 18.6 S·m$^{-1}$ and 0.6 S·m$^{-1}$, respectively (more than a 96% decrease, a 30× difference). The large difference in conductivity for solutions with low supporting electrolyte points to the possibility of enhanced electromigration when and where $Cu^{2+}$ is significantly depleted during electrodeposition.

Figure 2b shows a color map of solution pH for the same ranges of $CuSO_4$ and $H_2SO_4$ concentrations. The black contour lines are constant pH at the indicated values while the white contour lines show the fraction of sulfur containing species that exist as sulfate, i.e., $[SO_4^{2-}]/([HSO_4^-] + [SO_4^{2-}])$, the 0.5 case being equivalent to the transition point from a bisulfate to sulfate dominated electrolyte. Broadly speaking, the solution pH is determined by the concentration of sulfuric acid, as the black isocontour lines are generally close to vertical on the 2D plot. It is, nonetheless, interesting to consider the shift in the transition from primarily bisulfate to sulfate speciation as a function of the copper sulfate concentration. Literature sources indicate the $pK_a$ value for deprotonation of bisulfate[62] occurs at a pH value around 1.75; the present simulations yield a value of 1.66 when $CuSO_4$ concentration is set to zero. However, the sulfate anions from high concentrations of $CuSO_4$ substantially shift this value, resulting in a transition to a sulfate dominated species at a pH of −0.12 for a concentration of 0.88 mol·l$^{-1}$ $CuSO_4$. Although this study is focused on the electrical influence of sulfuric acid on feature filling, it must be noted that this observation raises questions regarding the influence of sulfate vs

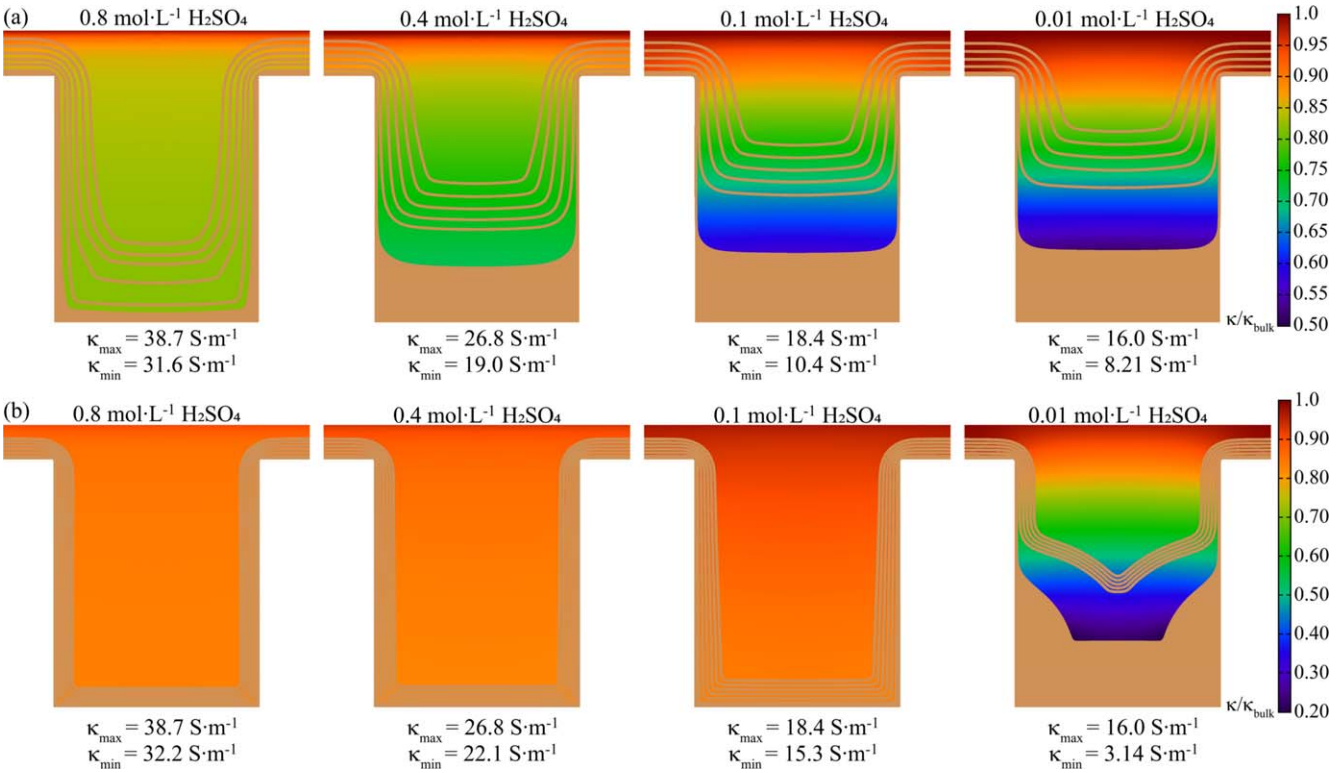


**Figure 4.** Simulations of galvanostatic copper electrodeposition after 30 min in microvias with a boundary layer thickness of 10 $\mu$m at the indicated sulfuric acid concentrations for (a) high-density ($R_c$ = 75 $\mu$m) spacing at a workpiece current density of $-204$ A·m$^{-2}$ and (b) low-density ($R_c$ = 750 $\mu$m) spacing at a workpiece current density of -76 A·m$^{-2}$. The color map represents normalized solution conductivity ($\kappa/\kappa_{bulk}$) after 5 min of deposition. Subsequent filling contours are spaced 5 min apart. The maximum conductivity ($\kappa_{max}$), equal to the bulk value, and the lowest conductivity at 5 min ($\kappa_{min}$) are indicated for each condition.

bisulfate on Cu electrodeposition both in the presence and absence of additive adsorption/desorption.

***Simulations of Cu electrodeposition in microvias.***—The influence of sulfuric acid concentration on electrolyte conductivity and feature filling is explored computationally in microvias having a 25 $\mu$m radius, 60 $\mu$m depth, and cell radius of 75 $\mu$m or 750 $\mu$m (referred to as high-density and low-density, respectively). The 2-D axisymmetric schematic is shown in Fig. 3a with the equipotential reference electrode (RE) and counter electrode (CE) plane positioned 0.25 cm away from the microvia field (located at $z = 0$). The impact of convective transport is inferred (i.e., implicit) by imposition of the specified boundary layer thickness $\delta$. Figure 3b shows a top-down schematic of the high-density and low-density configurations although the radial symmetry used in the simulations prevents exact comparison to the corresponding 2D geometry. The simulations detailed herein are galvanostatic so that varying the position of the RE/CE plane does not influence the growth dynamics of feature filling[57]; the applied electric potential simply adjusts to compensate for changes in the overall ohmic drop. Unless indicated otherwise, the electrolyte composition is 0.88 mol·l$^{-1}$ $CuSO_4$, 1 mmol·l$^{-1}$ NaCl, and 25 $\mu$mol·l$^{-1}$ poloxamine with the specified $H_2SO_4$ concentration.

Figure 4a shows simulations of the filling of high density microvias obtained after 5 min along with subsequent filling contours in 5 min intervals for galvanostatic Cu deposition at a workpiece current density of $-204$ A·m$^{-2}$ (defined as applied current scaled by the projected area of the computational cell) over a total of 30 min at the indicated concentrations of $H_2SO_4$. The color maps indicate normalized local solution conductivity ($\kappa/\kappa_{bulk}$) after 5 min of deposition. It is noteworthy that the deposit profile within the microvia after 5 min of deposition is substantially higher for concentrations of $H_2SO_4 \leqslant 0.4$ mol·l$^{-1}$; within this concentration range the deposit height is also incrementally higher with decreasing $H_2SO_4$ concentration. In general, the localized deposition in the lower acid concentrations ($\leqslant 0.4$ mol·l$^{-1}$) is fastest before 10 min, after which a transition to passive growth manifests in more conformal growth contours and thicker deposition on the field. The predicted contours for deposition in 0.8 mol·l$^{-1}$ $H_2SO_4$ are more uniformly spaced throughout the entire 30 min period of deposition, although slightly faster deposition occurs between 10 min and 20 min. The nonlinear transition in the growth profiles from essentially conformal filling with 0.8 mol·l$^{-1}$ $H_2SO_4$ to localized bottom-up filling with 0.4 mol·l$^{-1}$ $H_2SO_4$ qualitatively matches the experimental transition from conformal deposition to butterfly filling in THs over the same concentration range in Fig. 1a. Because the simulations are galvanostatic, the decrease in bulk conductivity $\kappa_{bulk}$ inherently produces higher potential gradients and thereby an increase in transport by electromigration. The decrease in $H_2SO_4$ concentration from 0.8 mol·l$^{-1}$ to 0.4 mol·l$^{-1}$, 0.1 mol·l$^{-1}$ and 0.01 mol·l$^{-1}$ reduces $\kappa_{bulk}$ by 31%, 53%, and 59%, respectively. Furthermore, due to $Cu^{2+}$ depletion at the depositing interface, a further decrease in *local* solution conductivity of 19%, 29%, 43%, and 49% from the respective bulk values is observed after 5 min. As depicted in Fig. 5 for $H_2SO_4$ concentrations of 0.01 mol·l$^{-1}$ and 0.8 mol·l$^{-1}$, these changes increase the potential gradient and enhance electromigration at the microvia bottom relative to the surrounding planar surface, increasing transport of cations towards, and anions away, from the microvia interface. Enhanced removal of the negatively charged $Cl^-$ ions from the surface destabilizes the inhibiting polymer-chloride adlayer and enhances transport of the positively charged $Cu^{2+}$ ions toward the surface. This results in further disruption of the inhibition layer, providing positive feedback that supports ongoing current localization to the most recessed

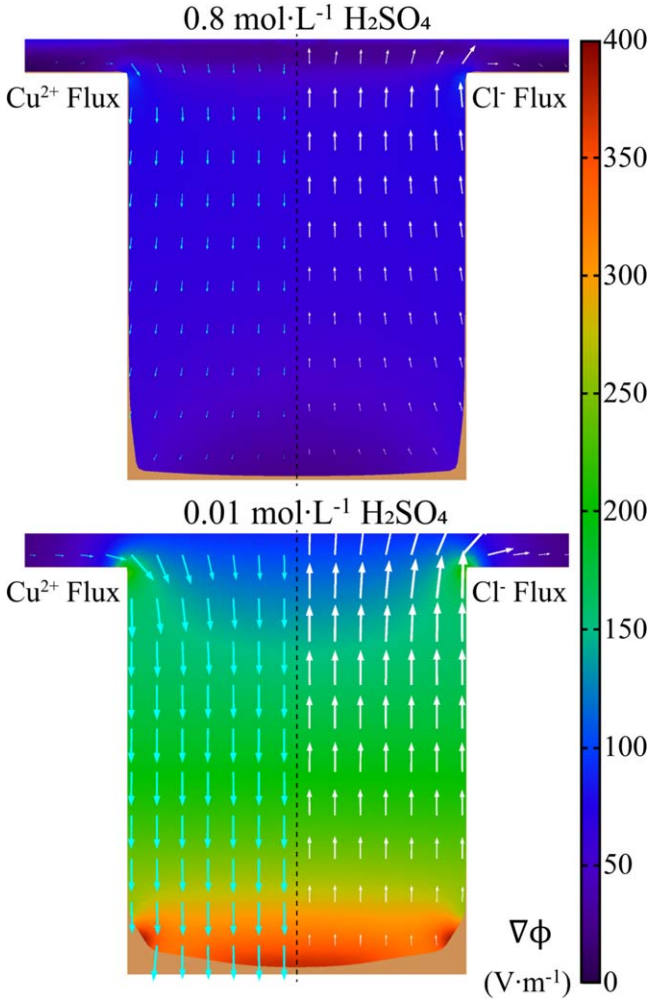


**Figure 5.** Simulations of galvanostatic copper electrodeposition in microvias at 1 min with a boundary layer thickness of 10 $\mu$m for the indicated $H_2SO_4$ concentrations for the high-density ($R_c$ = 75 $\mu$m) spacing at a workpiece current density of $-204$ A·m$^{-2}$. The color map represents the potential gradient at $t = 1$ min. Arrows show the electromigration component of the flux for $Cu^{2+}$ ions on the left-hand (cyan) and $Cl^-$ ions on the right-hand (white) sides of the via. The vector components are proportional to the ion flux with the same scaling-factor used for each ion in the maps for the two $H_2SO_4$ concentrations. Thus, the approximately 5× longer $Cu^{2+}$ arrows at the microvia bottom with 0.01 mol·l$^{-1}$ $H_2SO_4$ as compared to the simulation for 0.8 mol·l$^{-1}$ $H_2SO_4$ indicate a 5× higher electromigration component to the flux (specifically, 0.005 mol·(m$^2$·s)$^{-1}$ vs 0.001 mol·(m$^2$·s)$^{-1}$). Similarly, the 2× longer $Cl^-$ arrows at the microvia top in 0.01 mol·l$^{-1}$ $H_2SO_4$ as compared to the simulation for 0.8 mol·l$^{-1}$ $H_2SO_4$ correlate to a 2× higher electromigration component to the flux (specifically, $3.6 \times 10^{-6}$ mol·(m$^2$·s)$^{-1}$ vs $1.8 \times 10^{-6}$ mol·(m$^2$·s)$^{-1}$).

portion of the microvia. The vectors shown in Fig. 5 scale proportionally to the flux for the respective ion. Given the 1000× difference between the bulk $Cl^-$ concentrations of ≈ 1 mmol·l$^{-1}$ and $Cu^{2+}$ concentrations of ≈ 1 mol·l$^{-1}$ the scaling factor for the $Cl^-$ flux is ≈ 1000× larger than for the $Cu^{2+}$ flux to permit similar contrast.

Figure 4b shows simulations of galvanostatic deposition at a workpiece current density of $-76$ A·m$^{-2}$ for the same microvia dimensions and electrolyte composition as Fig. 4a but with the low-density ($R_c$ = 750 $\mu$m) via spacing. The trends are consistent with the high-density configuration: an increase in current localization to the microvia bottom as sulfuric acid concentration decreases. That said, the transition from conformal to bottom-up filling occurs at a lower $H_2SO_4$ concentration, between 0.1 mol·l$^{-1}$ and 0.01 mol·l$^{-1}$, with very little variation in the fill profiles for higher $H_2SO_4$ concentrations, and localization at the lower concentration manifests more as a passive-active transition along the sidewall and less as the horizontal profile of strictly bottom-up filling. The substantially greater decrease in local conductivity, to values as low as 3.14 S·m$^{-1}$ in the 0.01 mol·l$^{-1}$ $H_2SO_4$ solution after 5 min for the low-density features versus 8.21 S·m$^{-1}$ with the high density features, is also noteworthy; it is congruent with the greater cupric ion depletion derived from localization of the larger applied current as a result of the larger fraction of total area that is passive for the sparser via arrangement. The effect of varying the applied current was examined in 4 A·m$^{-2}$ increments. For low density features in 0.01 mol·l$^{-1}$ $H_2SO_4$, $-76$ A·m$^{-2}$ is the highest current density that yields seam- and void-free filling. Decreased acidity fosters localization of deposition to the microvia bottom but comes at a cost; the enhanced deposition rates deplete $Cu^{2+}$ enough to form seams and/or voids even at lower applied current densities. The maximum workpiece current densities for seam/void-free feature filling as a function of supporting electrolyte concentration in the solution are summarized in Table II for both via array patterns.

A more detailed view of current localization for the lowest and highest acidities is summarized in Fig. 6 for the microvia filling results shown in Fig. 4. For the high-density configuration in 0.01 mol·l$^{-1}$ $H_2SO_4$, shortly after current is applied (0 min) the ≈ $-200$ A·m$^{-2}$ of workpiece current density is distributed such that the local current density is ≈ $-1800$ A·m$^{-2}$ at the via bottom with only ≈ $-20$ A·m$^{-2}$ on the adjacent planar surface. Current localization is sustained until 4 min, from which time the current density at the via bottom steadily decreases in magnitude until it reaches a value of ≈ $-300$ A·m$^{-2}$ at 15 min. The majority of bottom-up filling occurs during this period, 33 $\mu$m over the first 10 min, with only 20 $\mu$m of further bottom-up filling over the remaining 20 min of the simulation although a difference of about 100 A·m$^{-2}$ between the via bottom and the surrounding field is sustained during this period. The 0.8 mol·l$^{-1}$ $H_2SO_4$ solution exhibits some localization of current initially as well, but current density at the via bottom only peaks at $-400$ A·m$^{-2}$ before quickly falling to a current density close to that on the field. Interestingly, at ≈ 10 min the conformal deposition shifts to a short period of current localization and accelerated deposition on the via bottom that peaks near ≈ $-900$ A·m$^{-2}$ before settling back to $-200$ A·m$^{-2}$ by 18 min. This is an example of the complex behavior that can occur when additive coverage is defined not only by incorporation related to the local metal deposition rate but also by additive and metal ion transport, themselves impacted by deposition and consumption throughout the filling feature. The same general behaviors are observed for the low density microvias in the low acid simulation in Fig. 6b, albeit somewhat more extreme. Current localization to the via bottom peaks near $-3{,}400$ A·m$^{-2}$

**Table II. Maximum workpiece current densities and fill-heights for seam-free, void-free filling in microvias.**

| | Maximum current density | | Fill height at Via center after 10 min | |
|---|---|---|---|---|
| $H_2SO_4$ Concentration | High-Density Via Pattern | Low-Density Via Pattern | High-Density Via Pattern | Low-Density Via Pattern |
| 0.8 mol·l$^{-1}$ | $-345$ A·m$^{-2}$ | $-204$ A·m$^{-2}$ | 15 $\mu$m | 14 $\mu$m |
| 0.4 mol·l$^{-1}$ | $-295$ A·m$^{-2}$ | $-127$ A·m$^{-2}$ | 31 $\mu$m | 23 $\mu$m |
| 0.1 mol·l$^{-1}$ | $-305$ A·m$^{-2}$ | $-89$ A·m$^{-2}$ | 46 $\mu$m | 24 $\mu$m |
| 0.01 mol·l$^{-1}$ | $-320$ A·m$^{-2}$ | $-76$ A·m$^{-2}$ | 50 $\mu$m | 28 $\mu$m |

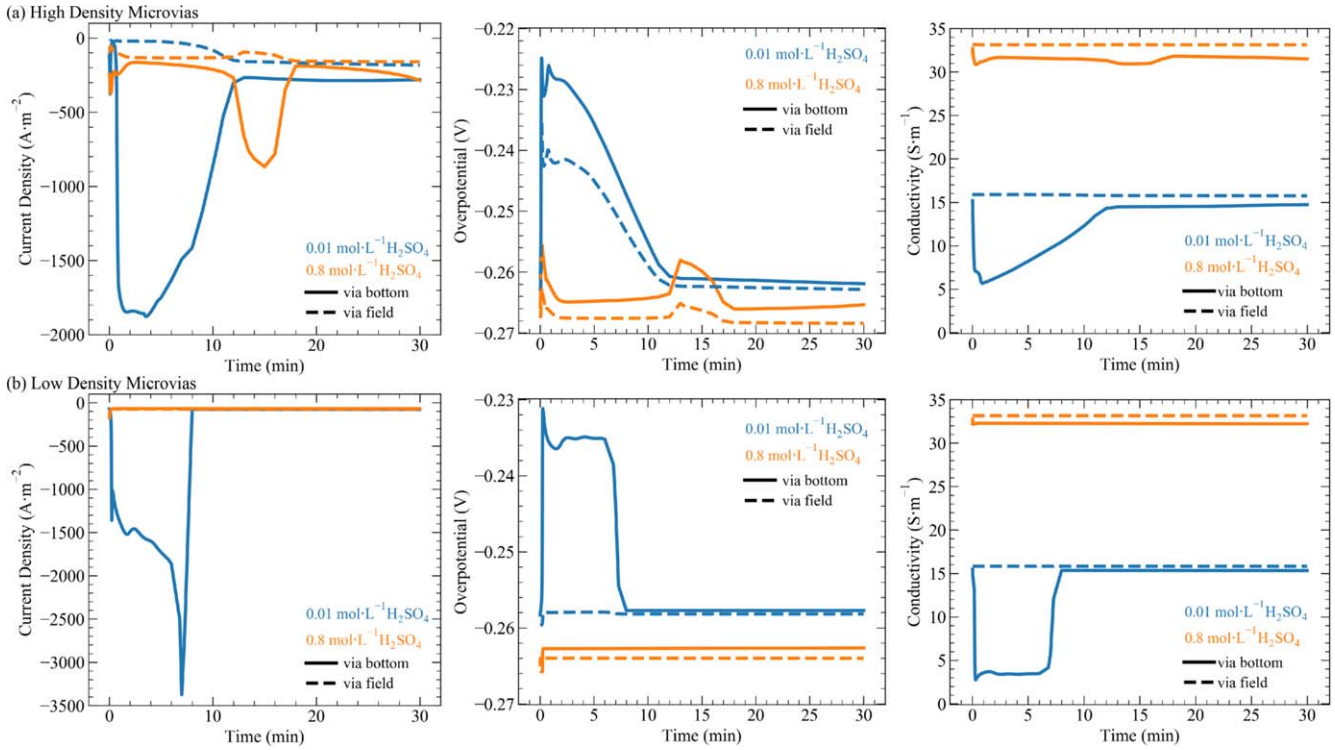


**Figure 6.** Transient current density, overpotential, and solution conductivity evaluated at the bottom of the unfilled region of the via (—) and at the field (specifically, cell radius edge) (—) for simulations in (a) high density and (b) low density microvias at the indicated concentrations of sulfuric acid. Simulations correspond to the profiles in Fig. 4.

while the surrounding field remains near $-75$ A·m$^{-2}$ for the entire simulation. For the high acid case, deposition is conformal for the entire simulation, exhibiting a minor difference between the microvia bottom and adjacent field of less than 10 A·m$^{-2}$ for most of the simulation. Interestingly, the low acid condition exhibits a much higher *local* current density for the sparse via arrangement relative to the higher density configuration despite the lower overall applied workpiece current density ($-76$ A·m$^{-2}$ vs $-204$ A·m$^{-2}$). This is because an overall higher *total* current ($-134$ $\mu$A vs $-3.6$ $\mu$A) is available for localization to the sparse via bottoms of the same dimension; the area of the via bottom represents 7.2% and 0.11% of the total electrode area for the high and low density configurations, respectively. This observation highlights the importance of considering pattern density effects in process optimization.

The overpotential transients in Fig. 6 show that an increase in current density at the via bottom is accompanied by relaxation in the reaction overpotential (i.e., shift to less negative values), a clear indicator of S-NDR type behavior. This is evident for both acidities and microvia configurations; although, like the current density transients, the overpotential difference between the via bottom and field is most significant for the low acid, low-density case. Local conductivity sampled at the center of the microvia bottom and on the field in Fig. 6 reveal the large difference in the variation, particularly during operation, between the high and low acid contents. The bulk solution conductivity decreases by 54% (a factor of 2.2×) when the sulfuric acid concentration is decreased from 0.8 mol·l$^{-1}$ to 0.01 mol·l$^{-1}$. For galvanostatic operation in a fixed electrochemical cell geometry this equates, to a first order approximation, to an equivalent 2.2× increase in transport by electromigration in the 0.01 mol·l$^{-1}$ $H_2SO_4$ solution. Even larger is the additional decrease in conductivity farther down the vias that arises from cupric ion depletion during active deposition at the via bottom in the low acid electrolyte. For both microvia configurations in the 0.8 mol·l$^{-1}$ $H_2SO_4$ solution, the maximum decrease in local conductivity between the field and microvia bottom is only about 8% to 12%. In contrast, in the 0.01 mol·l$^{-1}$ $H_2SO_4$ solution the conductivity decreases by a maximum of 64% and 83% (2.8× and 5.8× differences) for the high and low density configurations, respectively. There is an equivalent increase in contribution of electromigration to transport locally within the via bottom relative to the that above the feature.

Figure 7 shows the evolving concentrations of all ionic species as well as the ionic strength of the electrolyte immediately adjacent to the bottom (i.e., via center) of the advancing microvia surface in 0.01 mol·l$^{-1}$ $H_2SO_4$ for both high (Fig. 7a) and low (Fig. 7b) density configurations. In both configurations, the $Cu^{2+}$ concentration drops significantly at the start of deposition. In parallel, due to the demands of electroneutrality in Eq. 8 the concentration of the dominant anion, $SO_4^{2-}$, follows that of the $Cu^{2+}$, being transported away from the electrode through electromigration to match the spatial gradient of the $Cu^{2+}$ cation caused by the rapid deposition on the via bottom. Decrease of the $SO_4^{2-}$ concentration forces $HSO_4^-$ to dissociate, increasing the proton concentration and reducing the $HSO_4^-$ concentration as stipulated by the equilibrium condition in Eq. 3. Shortening of the via as deposition progresses up from the bottom gradually reduces the $Cu^{2+}$ concentration gradient within the via, increasing the cupric ion concentration at the bottom gradually for the high density configuration; the sudden decrease at approximately 7 min for the low density configuration reflects the halt of localized deposition that accompanies impingement of the deposits on the lower sidewalls immediately adjacent to the bottom surface (Fig. 4). In both cases, sulfate, proton, and bisulfate ions all adjust accordingly. Although not influenced by the homogeneous chemistry, both chloride and poloxamine (TET) concentrations shift due to the gradients created by incorporation with the growing solid and enhanced electromigration associated with the reduced local conductivity. This results in a 1 to 2 order of magnitude decrease of the negatively charged chloride concentration. The local concentration of the positively charged poloxamine, on the other hand, is actually increased slightly by electromigration, rising as high as 100 $\mu$mol·l$^{-1}$ before eventually falling back to the bulk concentration value of 25 $\mu$mol·l$^{-1}$. Although not shown, the high acid

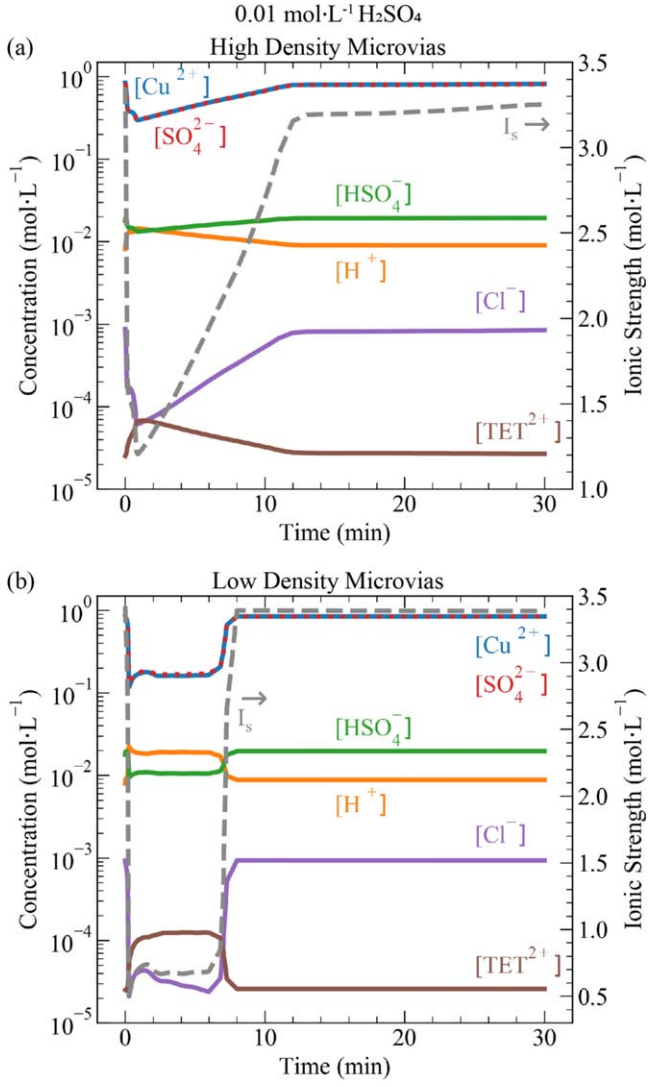


**Figure 7.** Transient species' concentrations at the microvia bottom in (a) high density and (b) low density microvias in 0.01 mol·l$^{-1}$ $H_2SO_4$. Ionic strength (—) calculated by Eq. 5 is also indicated.

(0.8 mol·l$^{-1}$ $H_2SO_4$) simulations indicate that $H^+$, $HSO_4^-$, and $SO_4^{2-}$ concentrations all adjust only slightly when $Cu^{2+}$ is depleted because their bulk concentrations, in the range 0.2 mol·l$^{-1}$ to 1.1 mol·l$^{-1}$, are of a similar magnitude.

***Simulations with reduced convective transport.***—The simulations in Figs. 4 through 7 approximate convective flow with a fixed boundary layer of 10 $\mu$m, roughly equivalent to that expected at the surface of a disk electrode rotating at 1600 rpm. Figure 8 shows simulations for the same electrolyte composition and applied currents as Fig. 4 but with a boundary layer thickness of 50 $\mu$m that corresponds to rotation at $\approx$ 60 rpm. Trends with the thicker boundary layer are generally consistent with those in Fig. 4, including the increased localization of current to the microvia bottom as $H_2SO_4$ concentration is reduced. That said, filling of the high-density features in Fig. 8a progresses substantially higher up the feature after 30 min of deposition. This is the result of weakened inhibitor (chloride and suppressor) flux given the longer, and thereby shallower, gradient across which additives must be supplied to replace those being consumed at the growing interface. The thicker boundary layer (decrease in convective transport) also reduces cupric ion transport, but the current densities selected in these simulations are not sufficiently large to result in voids or seams due to metal ion depletion. In sum, the reduced transport condition is advantageous for microvia filling. This observation brings into relief the utility of a variable transport condition (i.e., ramped or stepped) in experimental feature filling applications. In such a case, higher convection during early stages would favor the supply of metal ion to the recessed regions of the high-aspect ratio features while lower convection at later stages would enable higher filling by hindering reformation of the suppressor layer as the growing interface approaches the field.

The variation in fill height for low-density features with a 50 $\mu$m boundary layer thickness (Fig. 8b) relative to the 10 $\mu$m thickness (Fig. 4b) is even more substantial. With higher convection ($\delta$ = 10 $\mu$m) the transition between a passive growth profile and localized, bottom-up growth as a function of $H_2SO_4$ concentration occurred between 0.1 mol·l$^{-1}$ and 0.01 mol·l$^{-1}$. With lower convection ($\delta$ = 50 $\mu$m) this transition occurs between 0.8 mol·l$^{-1}$ and 0.4 mol·l$^{-1}$ $H_2SO_4$. The difference is due to enhanced impact of electromigration on the transport of all species as a result of more substantial cupric ion depletion for lower convection conditions. As such, a smaller drop in the supporting electrolyte concentration and conductivity is necessary to achieve bottom-up feature filling through dissimilar transport to the microvia bottom and the surrounding field. In all cases, the minimum conductivity $\kappa_{min}$ with $\delta$ = 50 $\mu$m is less than that with $\delta$ = 10 $\mu$m, achieving a decrease by 8× for the lowest $H_2SO_4$ concentration. The reduction in convection in 0.01 mol·l$^{-1}$ $H_2SO_4$ results in an increase in overall fill-height for the high density configuration relative to the $\delta$ = 10 $\mu$m condition in Fig. 4b. The effect is less significant in the low density configuration following the shift to conformal deposition.

***Effect of $CuSO_4$ concentration.***—The influence of supporting electrolyte on bottom-up fill is through enhanced transport by electromigration that is further amplified by the metal-ion and supporting electrolyte depletion gradients within the recessed microvia. Variation in the bulk $CuSO_4$ concentration is also expected to influence current localization to the microvia bottom. Simulations of the high density microvia configuration ($R_c$ = 75 $\mu$m) in Fig. 4a were repeated over a range of $CuSO_4$ concentrations for each of the $H_2SO_4$ concentrations examined previously. The results of simulations are summarized in Fig. 9, which shows the minimum height of the deposit within the microvia at 10 min as a function of $CuSO_4$ concentration. Over the range of $CuSO_4$ concentrations surveyed, the lowest acidity always yields the highest fill at 10 min. In fact, the simulation of 0.52 mol·l$^{-1}$ $CuSO_4$ and 0.01 mol·l$^{-1}$ $H_2SO_4$ has a higher fill after 10 min than all of the simulations for the range of $CuSO_4$ concentrations $<$ 0.92 mol·l$^{-1}$ when 0.8 mol·l$^{-1}$ $H_2SO_4$ is used as supporting electrolyte. The greatest difference in fill height between the highest and lowest $H_2SO_4$ concentrations examined occurs with 0.88 mol·l$^{-1}$ $CuSO_4$, the electrolyte for which the growth profiles are shown in Fig. 4a. Importantly, the more stable operation that is reflected in similarly high fill across a wider range of $CuSO_4$ concentrations with 0.01 mol·l$^{-1}$ $H_2SO_4$ in Fig. 9 might be helpful in the management of extended Cu electrodeposition operations. In particular, a decrease of the bulk concentration by 20% from 1 mol·l$^{-1}$ to 0.8 mol·l$^{-1}$ results in a significant loss of current localization manifest in much reduced fill height with the high acid electrolyte but relatively little variation in fill height for the low acid electrolyte. In a similar context, the advantage gained by reducing the supporting electrolyte concentration saturates, the difference between 0.01 mol·l$^{-1}$ to 0.1 mol·l$^{-1}$ at 0.88 mol·l$^{-1}$ $CuSO_4$ being only $\approx$ 2 $\mu$m. These combined attributes speak to the robustness of the feature filling capacity of the "*low acid—high copper*" chemistry to electrolyte depletion effects, albeit close attention to additive management is still required.

***Simulations of cyclic voltammetry.***—Figure 10 shows simulations of cyclic voltammetry for the different $H_2SO_4$ and $CuSO_4$ concentrations on a rotating disk electrode spinning at 100 rpm corresponding to an effective boundary layer thickness of 40 $\mu$m.

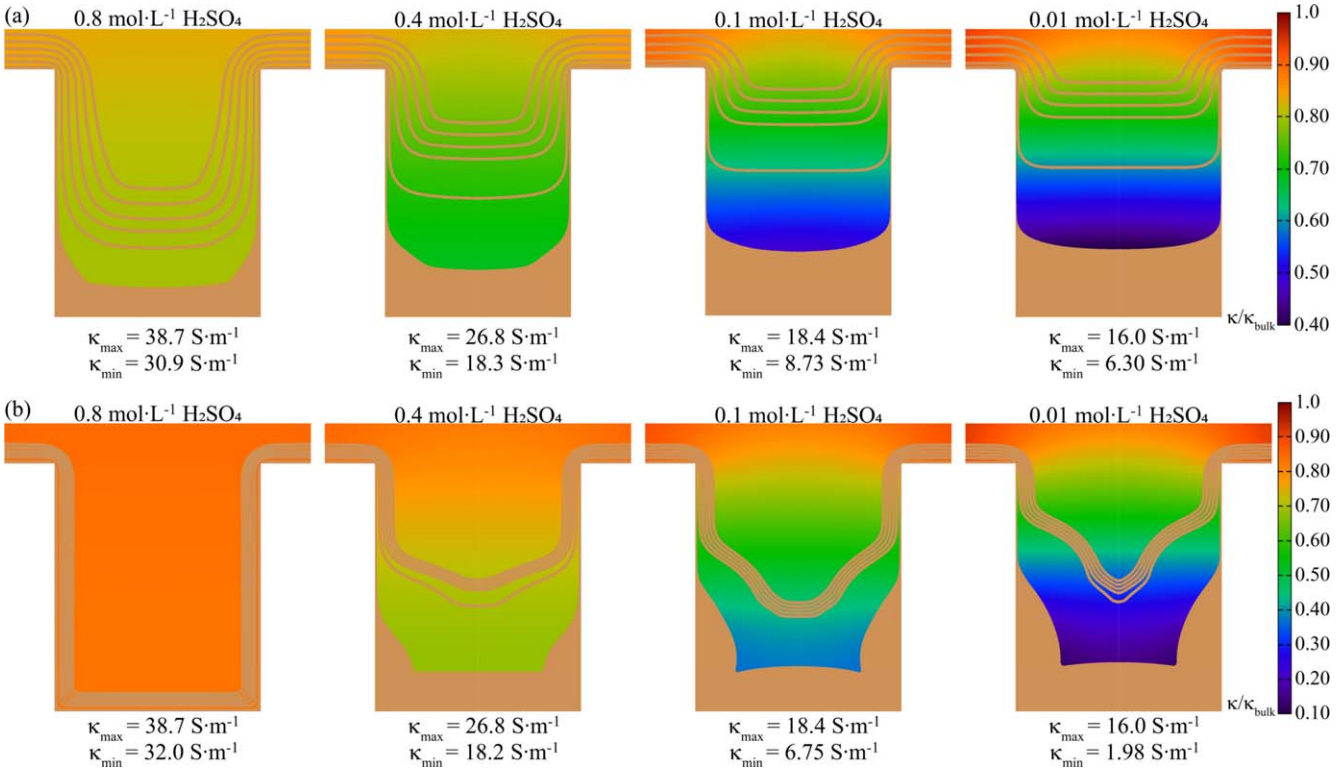


**Figure 8.** Simulations of galvanostatic copper electrodeposition after 30 min in microvias with a boundary layer thickness of 50 $\mu$m at the indicated sulfuric acid concentrations for (a) high-density ($R_c$ = 75 $\mu$m) spacing at a workpiece current density of -204 A·m$^{-2}$ and (b) low-density ($R_c$ = 750 $\mu$m) spacing at a workpiece current density of -72 A·m$^{-2}$. Reported values of current density are determined by the total applied current in the simulation scaled by the projected area of the simulated electrode ($A_{proj} = \pi R_c^2$). The color map represents normalized solution conductivity ($\kappa/\kappa_{bulk}$) after 5 min of deposition. Subsequent filling contours are spaced 5 min apart. The maximum conductivity ($\kappa_{max}$), which equals the bulk value, and the lowest conductivity at 5 min ($\kappa_{min}$) are indicated for each condition.

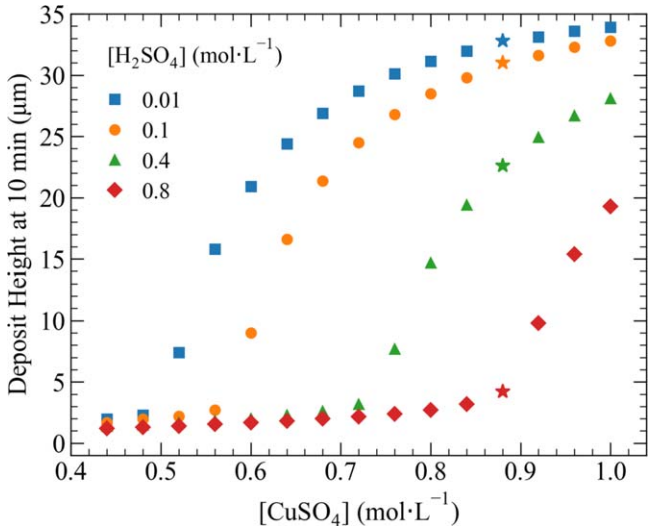


**Figure 9.** Plot of the minimum height of the deposit in the microvia after 10 min of deposition over a range of $CuSO_4$ concentrations with the indicated $H_2SO_4$ concentrations. Simulations are galvanostatic at a workpiece current density of $-204$ A·m$^{-2}$ in the high-density via ($R_c$ = 75 $\mu$m) configuration with a boundary layer thickness of 10 $\mu$m. Stars represent the conditions in Fig. 4a.

Voltammetry based on the combined reference/counter electrode positioned 0.31 cm away from the working electrode is shown by the dashed lines. For the 0.88 mol·l$^{-1}$ $CuSO_4$ based electrolyte the bulk cell resistances are 9 Ω and 4 Ω for 0.01 mol·l$^{-1}$ and 0.8 mol·l$^{-1}$ $H_2SO_4$, respectively. Hysteresis associated with breakdown of the polyether-halide suppressor layer is present for both acid concentrations. However, ohmic losses due to the finite electrolyte conductivity impact the overpotential at the working electrode and lead to significant distortions from the intended triangular waveform of the applied overpotential. For the low acid electrolyte, a transport limited current is not reached due to the significant and increasing contribution of electromigration. Further still, the concentration gradients, including those that develop to maintain electroneutrality, lead to further increases in resistivity and thereby ohmic losses. If the distance between reference and working electrodes is increased by a factor of 3.2× the CV sweeps (translucent solid lines) are almost linear, reflecting electrolyte resistance that dominates the response over the non-linear kinetics associated with charge transfer reactions and suppressor additive dynamics. The above distortions speak to the non-trivial nature of making effective electroanalytical measurements and extracting robust rate constants for kinetics in processes utilizing such resistive media.

Post-experiment correction for the ohmic losses, applied only to the negative-going sweeps, reveals the importance of $CuSO_4$ concentration in expressing S-NDR behavior that underlies bottom-up feature filling. With the 0.88 mol·l$^{-1}$ $CuSO_4$ electrolytes the inversion is evident, with the difference between the local min and max potentials on the S-shaped curves being 22 mV and 8 mV for the 0.01 mol·l$^{-1}$ and 0.8 mol·l$^{-1}$ $H_2SO_4$ solutions, respectively. With the more dilute 0.44 mol·l$^{-1}$ $CuSO_4$ electrolytes, the low acid condition reveals an inversion of only 3 mV while the high acid condition exhibits no S-NDR inversion at all. Accordingly, simulations of feature filling exhibit no localization of current to the feature bottom in 0.44 mol·l$^{-1}$ $CuSO_4$ electrolytes (also evident in Fig. 9). Importantly, in contrast to most post-experimental iR-corrections, the iR-corrections in Fig. 10 utilize the *instantaneous* solution

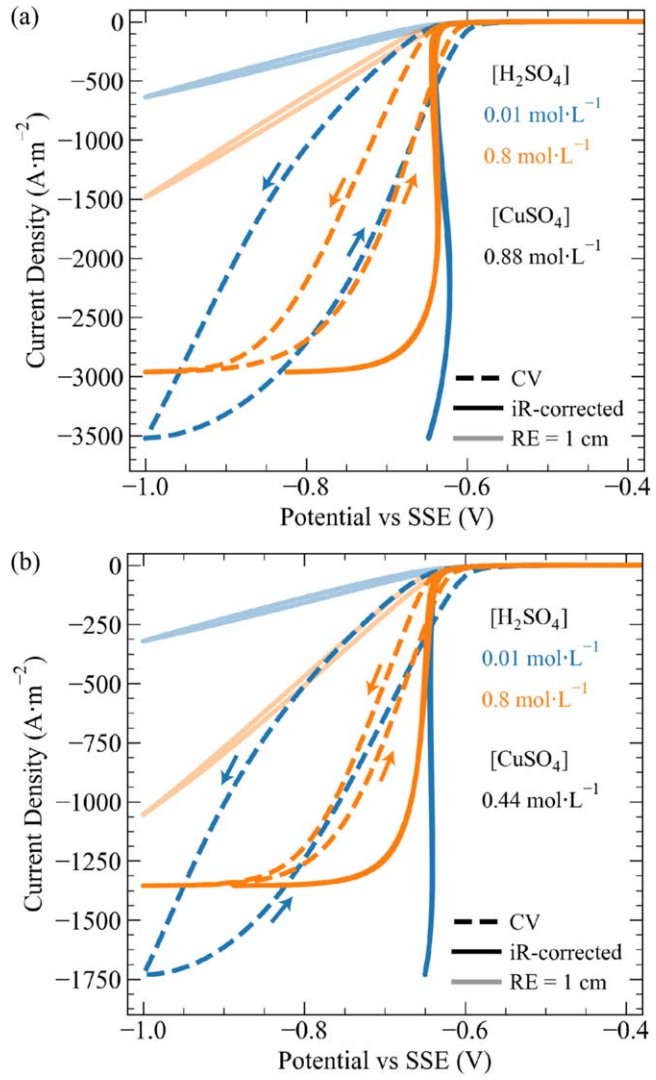


**Figure 10.** Simulations of cyclic voltammetry (CV, —) at 2 mV·s$^{-1}$ at the indicated concentrations of $H_2SO_4$ with a reference electrode position of 0.325 cm in (a) 0.88 mol·l$^{-1}$ and (b) 0.44 mol·l$^{-1}$ $CuSO_4$. Post-experimental correction for ohmic losses (—) reveals the characteristic negative differential resistance. Simulations with a reference electrode position of 1 cm show the linear nature of CV for systems producing high currents.

resistance rather than the steady-state bulk resistance; they thus account for variations in cell resistance as a function of applied potential including the contribution of electrolyte depletion.

## Conclusions

Simulations of S-NDR derived superconformal Cu electrodeposition in microvias demonstrate enhanced current localization and bottom-up filling as the concentration of the supporting electrolyte is decreased. This result is directly related to a drop in local electrolyte conductivity where metal ion is depleted, occurring most substantially in the most recessed regions of the microvia due to constraints on diffusive and convective mass transport as well as the demands of electroneutrality within the electrolyte. For $CuSO_4$–$H_2SO_4$ electrolytes with high sulfuric acid concentrations the current is primarily supported by $H^+$, $HSO_4^-$, and $SO_4^{2-}$ so that depletion of the $Cu^{2+}$ ion concentration does not significantly alter electrolyte conductivity. With low acid concentrations the current is primarily supported by the $Cu^{2+}$ and $SO_4^{2-}$ so that metal ion depletion through the Cu electrodeposition reaction can significantly reduce local electrolyte conductivity. The impact of the $Cu^{2+}$ depletion is compounded by the 1:1 reduction of $SO_4^{2-}$ concentration that accompanies it due to electroneutrality. As a result, simulations presented here exhibit as much as an eight-fold reduction in local conductivity in the electrolyte adjacent to the growing interface for solutions with 0.01 mol·l$^{-1}$ $H_2SO_4$. With $Cu^{2+}$ depletion greatest within filling microvias, the conductivity drop helps to further localize bottom-up deposition within the via. Stabilization of the bottom-up filling dynamic is also derived from migration of the kinetically suppressing $Cl^-$ additive away from, and the kinetically activating $Cu^{2+}$ ion toward, the actively depositing via bottom.

Simulations indicate that the feature filling advantage gained through reduced supporting electrolyte concentration depends on the spacing of the individual microvias (i.e., feature density). Specifically, the high density features ($R_c$ = 75 $\mu$m) explored here exhibit a more gradual enhancement in current localization and fill height as $H_2SO_4$ concentration is reduced from 0.8 mol·l$^{-1}$ to 0.01 mol·l$^{-1}$ in electrolyte with 0.88 mol·l$^{-1}$ $CuSO_4$. The low density features ($R_c$ = 750 $\mu$m) show entirely conformal growth at concentrations $\geqslant$ 0.1 mol·l$^{-1}$ $H_2SO_4$ while bottom-up growth is only operational at 0.01 mol·l$^{-1}$ $H_2SO_4$. The impact of feature density is related to the ratio of passive area (field) to active area (microvia bottom) as well as the boundary layer that defines transport. With a boundary layer of 50 $\mu$m the transition between conformal growth and bottom-up fill occurs between 0.8 mol·l$^{-1}$ and 0.4 mol·l$^{-1}$ $H_2SO_4$ for the low-density features. With lower levels of diffusive/convection mass transport a smaller deviation in local conductivity is needed to bias current to the bottom of the microvia. The metal ion content also influences the level of current localization and bottom-up fill.

Taken together these results provide substantial understanding and guidance regarding optimization of bottom-up filling processes in additive suppressed binary electrolyte systems. This exploration focused on the electrical nature of reduced supporting electrolyte; additional questions remain regarding the influence, significant or otherwise, of increased pH or local anion content (i.e., $SO_4^{2-}$) on chemical interactions between surface adsorbates and the solvated metal ion.

## Acknowledgments

NIST acknowledges partial support from DuPont Electronics and Imaging, Marlborough, MA 01752. We acknowledge the efforts of Andrew Ericks in helping generate some of the data in Fig. 2b while participating in the NIST Summer Undergraduate Research Fellowship Program during the summer of 2017.

## ORCID

T. M. Braun https://orcid.org/0000-0002-9779-3785
D. Josell https://orcid.org/0000-0002-4273-1923
T. P. Moffat https://orcid.org/0000-0003-4377-1692

## References

1. S. K. Kim, D. Josell, and T. P. Moffat, *J. Electrochem. Soc.*, **153**, C616 (2006).
2. S. K. Kim, D. Josell, and T. P. Moffat, *J. Electrochem. Soc.*, **153**, C826 (2006).
3. T. P. Moffat, D. Wheeler, M. D. Edelstein, and D. Josell, *IBM J. Res. Dev.*, **49**, 19 (2005).
4. T. P. Moffat, D. Wheeler, and D. Josell, *J. Electrochem. Soc.*, **151**, C262 (2004).
5. T. P. Moffat, J. E. Bonevich, W. H. Huber, A. Stanishevsky, D. R. Kelly, G. R. Stafford, and D. Josell, *J. Electrochem. Soc.*, **147**, 4524 (2000).
6. M. A. Pasquale, L. M. Gassa, and A. J. Arvia, *Electrochim. Acta*, **53**, 5891 (2008).
7. M. Tan, C. Guymon, D. Wheeler, and J. N. Harb, *J. Electrochem. Soc.*, **154**, D78 (2007).
8. P. Broekmann, A. Fluegel, C. Emnet, M. Arnold, C. Roeger-Goepfert, A. Wagner, H. T. M. Nguyen, and D. Mayer, *Electrochim. Acta*, **56**, 4724 (2011).
9. P. M. Vereecken, R. A. Binstead, H. Delgianni, and P. C. Andricacos, *IBM J. Res. Dev.*, **49**, 3 (2005).
10. M. Tan and J. N. Harb, *J. Electrochem. Soc.*, **150**, C420 (2003).
11. C. H. Chen, C. W. Lu, S. M. Huang, and W. P. Dow, *Electrochim. Acta*, **56**, 5954 (2011).
12. W. P. Dow, H. S. Huang, and Z. Lin, *Electrochem. Solid St.*, **6**, C134 (2003).
13. D. Josell, L. A. Menk, A. E. Hollowell, M. Blain, and T. P. Moffat, *J. Electrochem. Soc.*, **166**, D3254 (2019).

14. D. Josell and T. P. Moffat, *J. Electrochem. Soc.*, **165**, D23 (2018).
15. T. P. Moffat and D. Josell, *J. Electrochem. Soc.*, **159**, D208 (2012).
16. T. M. Braun, D. Josell, M. Silva, J. Kildon, and T. P. Moffat, *J. Electrochem. Soc.*, **166**, D3259 (2019).
17. W. P. Dow, H. H. Chen, M. Y. Yen, W. H. Chen, K. H. Hsu, P. Y. Chuang, H. Ishizuka, N. Sakagawa, and R. Kimizuka, *J. Electrochem. Soc.*, **155**, D750 (2008).
18. W. P. Dow, D. H. Liu, C. W. Ku, C. H. Chen, J. J. Yan, and S. M. Huang, *Electrochem. Solid St.*, **14**, D13 (2011).
19. G. Y. Lin, J. J. Yan, M. Y. Yen, W. P. Dow, and S. M. Huang, *J. Electrochem. Soc.*, **160**, D3028 (2013).
20. P. Ogutu, E. Fey, and N. Dimitrov, *J. Electrochem. Soc.*, **162**, D457 (2015).
21. T. M. Braun, S. H. Kim, H. J. Lee, T. P. Moffat, and D. Josell, *J. Electrochem. Soc.*, **165**, D291 (2018).
22. D. Josell and T. P. Moffat, *J. Electrochem. Soc.*, **163**, D322 (2016).
23. D. Josell, M. Silva, and T. P. Moffat, *J. Electrochem. Soc.*, **163**, D809 (2016).
24. D. Josell and T. P. Moffat, *J. Electrochem. Soc.*, **164**, D327 (2017).
25. D. Josell and T. P. Moffat, *J. Electrochem. Soc.*, **160**, D3035 (2013).
26. L. Yang, A. Radisic, J. Deconinck, and P. M. Vereecken, *J. Electrochem. Soc.*, **161**, D269 (2014).
27. G.-K. Liu, S. Zou, D. Josell, L. J. Richter, and T. P. Moffat, *J. Phys. Chem. C*, **122**, 21933 (2018).
28. M. Yokoi, S. Konishi, and T. Hayashi, *Denki Kagaku*, **52**, 218 (1984).
29. Z. V. Feng, X. Li, and A. A. Gewirth, *J. Phys. Chem. B*, **107**, 9415 (2003).
30. M. Yokoi, S. Konishi, and T. Hayashi, *Denki Kagaku*, **51**, 460 (1983).
31. J. P. Healy, D. Pletcher, and M. Goodenough, *J. Electroanal. Chem.*, **338**, 155 (1992).
32. J. J. Kelly and A. C. West, *J. Electrochem. Soc.*, **145**, 3472 (1998).
33. K. Doblhofer, S. Wasle, D. M. Soares, K. G. Weil, and G. Ertl, *J. Electrochem. Soc.*, **150**, C657 (2003).
34. K. R. Hebert, *J. Electrochem. Soc.*, **152**, C283 (2005).
35. K. R. Hebert, S. Adhikari, and J. E. Houser, *J. Electrochem. Soc.*, **152**, C324 (2005).
36. M. L. Walker, L. J. Richter, and T. P. Moffat, *J. Electrochem. Soc.*, **152**, C403 (2005).
37. W. P. Dow, M. Y. Yen, W. B. Lin, and S. W. Ho, *J. Electrochem. Soc.*, **152**, C769 (2005).
38. M. J. Willey and A. C. West, *J. Electrochem. Soc.*, **153**, C728 (2006).
39. M. J. Willey and E. J. McInerney, *J. Electrochem. Soc.*, **156**, D98 (2009).
40. M. E. Huerta-Garrido and M. D. Pritzker, *J. Electrochem. Soc.*, **156**, D175 (2009).
41. M. E. Huerta-Garrido and M. D. Pritzker, *J. Electrochem. Soc.*, **156**, D36 (2009).
42. M. R. Hill and G. T. Rogers, *J. Electroanal. Chem.*, **86**, 179 (1978).
43. M. Hayase, M. Taketani, T. Hatsuzawa, and K. Hayabusa, *Electrochem. Solid St.*, **6**, C92 (2003).
44. D. Josell, D. Wheeler, and T. P. Moffat, *J. Electrochem. Soc.*, **159**, D570 (2012).
45. D. Wheeler, T. P. Moffat, and D. Josell, *J. Electrochem. Soc.*, **160**, D3260 (2013).
46. L. Yang, A. Radisic, J. Deconinck, and P. M. Vereecken, *J. Electrochem. Soc.*, **160**, D3051 (2013).
47. L. A. Menk, D. Josell, T. P. Moffat, E. Baca, M. G. Blain, A. Smith, J. Dominguez, J. McClain, P. D. Yeh, and A. E. Hollowell, *J. Electrochem. Soc.*, **166**, D3066 (2019).
48. T. M. Braun, D. Josell, J. John, S. Deshpande, and T. P. Moffat, *J. Electrochem. Soc.*, **167**, 162508 (2020).
49. I. Krastev and M. T. Koper, *Physica A*, **213**, 199 (1995).
50. J. Jorne and M. G. Lee, *J. Electrochem. Soc.*, **143**, 865 (1996).
51. K. Krischer, *J. Electroanal. Chem.*, **501**, 1 (2001).
52. Y. J. Li, J. Oslonovitch, N. Mazouz, F. Plenge, K. Krischer, and G. Ertl, *Science*, **291**, 2395 (2001).
53. N. Mazouz and K. Krischer, *J. Phys. Chem. B*, **104**, 6081 (2000).
54. K. Krischer, N. Mazouz, and G. Flatgen, *J. Phys. Chem. B*, **104**, 7545 (2000).
55. L. A. Menk, E. Baca, M. G. Blain, J. McClain, J. Dominguez, A. Smith, and A. E. Hollowell, *J. Electrochem. Soc.*, **166**, D3226 (2019).
56. T. M. Braun, D. Josell, and T. P. Moffat, *J. Electrochem. Soc.*, **167**, 082509 (2020).
57. T. M. Braun, D. Josell, and T. P. Moffat, *Electrochim. Acta*, **375**, 137925 (2021).
58. S. K. Cho, M. J. Kim, and J. J. Kim, *Electrochem. Solid St.*, **14**, D52 (2011).
59. P. J. Tao, Y. G. Chen, W. T. Cai, and Z. G. Meng, *J. Materials*, **14**, 1 (2021).
60. T. M. Braun, D. Josell, J. John, and T. P. Moffat, *J. Electrochem. Soc.*, **167**, 013510 (2020).
61. A. J. Bard and L. R. Faulkner, *Electrochemical Methods: Fundamentals and Applications* (Wiley, Hoboken, NJ) 3rd ed. (2004).
62. J. M. Casas, F. Alvarez, and L. Cifuentes, *Chem. Eng. Sci.*, **55**, 6223 (2000).
63. J. M. Casas, F. Alvarez, G. Crisostomo, L. Cifuentes, and G. Cifuentes, *4th International Conference of the COPPER99/COBRE99*, Phoenix, AZ, Oct. 10–13, 1999, ed. S. K. Young, D. B. Dreisinger, R. P. Hackl, and D. G. Dixon (Hydrometallurgy of Copper) **99** (1999).
64. J. Gonzalez-Lopez, C. Alvarez-Lorenzo, P. Taboada, A. Sosnik, I. Sandez-Macho, and A. Concheiro, *Langmuir*, **24**, 10688 (2008).
65. T. I. Quickenden and Q. Z. Xu, *J. Electrochem. Soc.*, **143**, 1248 (1996).
66. J. S. Newman, *Electrochemical Systems* (Wiley, Hoboken, NJ) (2004).
67. R. A. Waggoner, F. D. Blu, and J. C. Lang, *Macromolecules*, **28**, 2658 (1995).
68. L. Masaro, X. X. Zhu, and P. M. Macdonald, *Macromolecules*, **31**, 3880 (1998).
69. K. Shimada, H. Kato, T. Saito, S. Matsuyama, and S. Kinugasa, *J. Chem. Phys.*, **122** (2005).
70. J. F. Dong, J. Armstrong, B. Z. Chowdhry, and S. A. Leharne, *Thermochim. Acta*, **417**, 201 (2004).
71. O. M. Magnussen, *Chem. Rev.*, **102**, 670 (2002).
72. D. Fraenkel, *New J. Chem.*, **39**, 5124 (2015).
73. I. Puigdomenech, *Chemical Equilibrium Diagrams* (Inorganic Chemistry Royal Institute of Technology (KTH), Stockholm, Sweden) (2004).